remote sensing

Article

Space-Time Adaptive Processing Clutter-Suppression Algorithm Based on Beam Reshaping for High-Frequency Surface Wave Radar

Jiaming Li, Qiang Yang, Xin Zhang *, Xiaowei Ji and Dezhu Xiao

School of Electronics and Information Engineering, Harbin Institute of Technology, Harbin 150001, China; 18b905030@stu.hit.edu.cn (J.L.); yq@hit.edu.cn (Q.Y.); 20b905053@stu.hit.edu.cn (X.J.); 21b905050@stu.hit.edu.cn (D.X.)
* Correspondence: zhangxinhit@hit.edu.cn; Tel.: +86-186-4658-1310

Abstract: In high-frequency surface wave radar (HFSWR) systems, clutter is a common phenomenon that causes objects to be submerged. Space-time adaptive processing (STAP), which uses two-dimensional data to increase the degrees of freedom, has recently become a crucial tool for clutter suppression in advanced HFSWR systems. However, in STAP, the pattern is distorted if a clutter component is contained in the main lobe, which leads to errors in estimating the target angle and Doppler frequency. To solve the main-lobe distortion problem, this study developed a clutter-suppression method based on beam reshaping (BR). In this method, clutter components were estimated and maximally suppressed in the side lobe while ensuring that the main lobe remained intact. The results of the proposed algorithm were evaluated by comparison with those of standard STAP and sparse-representation STAP (SR-STAP). Among the tested algorithms, the proposed BR algorithm had the best suppression performance and the most accurate main-lobe peak response, thereby preserving the target angle and Doppler frequency information. The BR algorithm can assist with target detection and tracking despite a background with ionospheric clutter.

Keywords: high-frequency radar; space-time adaptive processing; clutter suppression; beam reshaping; sparse representation; signal processing

check for updates

Citation: Li, J.; Yang, Q.; Zhang, X.; Ji, X.; Xiao, D. Space-Time Adaptive Processing Clutter-Suppression Algorithm Based on Beam Reshaping for High-Frequency Surface Wave Radar. *Remote Sens.* **2022**, *14*, 2935. https://doi.org/10.3390/rs14122935

Academic Editor: Silvia Piedracoba

Received: 17 May 2022
Accepted: 15 June 2022
Published: 19 June 2022

1. Introduction

High-frequency surface wave radars (HFSWRs) exhibit high performance in over-horizon detection, and have become crucial tools to monitor maritime targets by using the high-frequency (HF) band of 3–30 MHz [1–4]. In the HF band, echoes are highly complex and contain space-spread clutter, such as sea clutter and ionospheric clutter [5]. Ionospheric clutter includes echoes originating from single or multiple ionospheric layers, and the resulting propagation strongly depends on the HF radar signals [6,7]. This clutter is typically nonhomogeneous and has higher energy than those of general targets, which can seriously affect target detection [8]. Thus, methods to suppress ionospheric clutter and guarantee submerged target detection have been topics of interest [9–11].

In particular, for space-spread clutter, one-dimensional processing is not applicable in a complex environment due to the low degrees of freedom (DOF). In [12,13], one-dimensional processing was converted to two-dimensional processing via space-time adaptive processing (STAP) to increase the DOF of the system. A joint domain localised (JDL) method was proposed in [14] to enhance the applicability of STAP to HFSWR to reduce the computational cost. Many methods have been proposed to improve the STAP performance in nonhomogeneous environments, such as the generalised inner product (GIP) algorithm [15], power selected training (PST) algorithm [16], and sparse-representation STAP (SR-STAP) algorithm [17].

The key step of STAP is to estimate the covariance matrix by utilizing selected independent, identically distributed training samples with the clutter components. However, during the covariance matrix estimation, clutter components in the main lobe of the adaptive weight vector can lead to its deformation, resulting in a loss of the target's angle and Doppler frequency information after STAP processing. To solve this problem, this paper proposes a clutter-suppression method based on beam reshaping (BR) that estimates and maximally suppresses the clutter components in the side lobe while ensuring that the main lobe remains intact, thereby preserving the target angle and Doppler frequency information.

The main contributions are described as follows:

1. The influence of main-lobe clutter on STAP was analysed by formula derivations and simulation results. The results confirmed that main-lobe clutter could seriously influence the adaptive weight vector beam pattern of STAP by distorting the beam pattern and reducing the spatial gain.

2. A sparse-representation algorithm was used to estimate the clutter principal components, and the main and side lobe were classified for subsequent calculation. Then, a clutter-suppression method was proposed based on BR that maximally suppressed the clutter components in the side lobe while ensuring that the main lobe remained intact, thereby preserving the target angle and Doppler frequency information.

3. In addition, compared to standard STAP and SR-STAP, the proposed algorithm provided a more accurate angle–frequency response, which met the requirements of a maximum target response and a notch response with side-lobe clutter, particularly in the angle domain.

The remainder of this paper is organised as follows: Section 2 introduces the data model and conventional STAP algorithm principle for HFSWR and explains the cause of the main-lobe target information distortion and loss that are caused by clutter components during STAP processing. Section 3 presents a method to estimate the space-time spectrum of HFSWR based on sparse representation [16]. Section 4 presents a clutter-suppression algorithm based on BR to solve the main-lobe distortion problem in conventional STAP. Section 5 describes the simulation results of the proposed algorithm based on measured data from ionosphere clutter data, and presents an analysis of the experimental results. Finally, Section 6 presents the conclusions of this study.

2. STAP Algorithm in HFSWR

2.1. Signal Model and Basic Principle of STAP in HFSWR

The HFSWR system is assumed to comprise a uniform linear array consisting of N_e elements with a spacing of d between the array elements. The coherent integration time contains N_p signal pulses with a sampling frequency f_s. Hence, a data vector $\boldsymbol{X}_l \in \mathbb{C}^{M\times 1}$ of $M = N_e N_p$ dimensions can be obtained for the l_{th} range bin as follows:

$$\boldsymbol{X}_l = [\boldsymbol{x}_1\ \boldsymbol{x}_2\ \ldots\ \boldsymbol{x}_{N_e}]^{\mathrm{T}}, \tag{1}$$

$$\boldsymbol{x}_q = \left[x_{q,1}\ x_{q,2}\ \ldots\ x_{q,N_p}\right], q = 1, 2, \ldots, N_e \tag{2}$$

The space-time steering vector of the target echo is defined as follows:

$$\boldsymbol{v}(f_t, \phi_t) = \boldsymbol{b}(f_t) \otimes \boldsymbol{a}(\phi_t), \tag{3}$$

where $\boldsymbol{a}(\phi_t) = \left[1\ Z_s\ \cdots\ Z_s^{N_e-1}\right]^T$ is the space steering vector, $\boldsymbol{b}(f_t) = \left[1\ Z_t\ \cdots\ Z_t^{N_p-1}\right]^T$ is the time steering vector, and $\otimes$ is the Kronecker product. Thus, $v \in \mathbb{C}^{M\times 1}$. Additionally, $Z_s = e^{j2\pi(d/\lambda)\sin\phi_t}$ and $Z_t = e^{j2\pi(f_t/f_R)}$, where λ is the wavelength of the transmitting signal, ϕ_t is the target direction of arrival, f_t is the target Doppler frequency, $f_R = 1/t_m$ is the signal pulse repetition frequency, and t_m coherent integration time.

Subsequently, the received data can be expressed as the sum of the target signal, clutter, and noise as follows:

$$\boldsymbol{X}_l = \xi_t \boldsymbol{v}(f_t, \phi_t) + \boldsymbol{c} + \boldsymbol{n}, \tag{4}$$

where ξ_t is the amplitude of the target, $\boldsymbol{c}$ is the ionospheric clutter, and $\boldsymbol{n}$ is noise.

The principal step of the STAP method involves the determination of an optimal weight vector $\boldsymbol{v}_{stap}$ to suppress clutter:

$$\boldsymbol{y} = \boldsymbol{v}_{stap}{}^{\mathrm{H}} \boldsymbol{X}_l, \tag{5}$$

where $[\bullet]^{\mathrm{H}}$ is the conjugate transpose and $\boldsymbol{y}$ is the STAP output.

In the optimised STAP method, the adaptive weight vector can be calculated as follows:

$$\boldsymbol{v}_{stap} = \mathbf{R}^{-1} \boldsymbol{v}, \tag{6}$$

where $\mathbf{R}$ is the covariance matrix of the clutter and noise. For a real system, $\mathbf{R}$ must be provided as prior information or estimated using sample data as follows:

$$\mathbf{R} = \frac{1}{L} \sum_{1}^{L} \boldsymbol{X}_l \boldsymbol{X}_l^{\mathrm{H}}, \tag{7}$$

where L is the number of training samples and $l = [1, 2, \ldots, L]$. The training sample $\boldsymbol{X}_l$ used here should not contain the target component. It is difficult to collect enough training samples that conform to the independent identical distribution in a complex ionospheric clutter background.

2.2. Performance Analysis of STAP with Main-Lobe Clutter Component

Assuming the training sample has one clutter component, the covariance matrix $\mathbf{R}$ can be expressed as follows:

$$\mathbf{R} = \sigma_n^2 \mathbf{I} + \mathbf{R}_c, \tag{8}$$

where σ_n^2 is the variance of the noise and $\mathbf{I}$ is the identity matrix. Thus, the covariance matrix of the clutter is expressed as follows:

$$\mathbf{R}_c = P_c \boldsymbol{v}(f_c, \phi_c) \boldsymbol{v}^{\mathrm{H}}(f_c, \phi_c), \tag{9}$$

where P_c is the power of the clutter and $\boldsymbol{v}(f_c, \phi_c)$ is the space-time steering vector of the clutter component. Because $\mathbf{R}_c$ is a Hermite matrix, the inverse of $\mathbf{R}$ is expressed as follows:

$$\mathbf{R}^{-1} = \frac{1}{\sigma_n^2} \left[\mathbf{I} - \frac{\frac{1}{\sigma_n^2} P_c \boldsymbol{v}(f_c, \phi_c) \boldsymbol{v}^{\mathrm{H}}(f_c, \phi_c)}{1 + \frac{P_c}{\sigma_n^2} \boldsymbol{v}^{\mathrm{H}}(f_c, \phi_c) \boldsymbol{v}(f_c, \phi_c)} \right] = \frac{1}{\sigma_n^2} \left[\mathbf{I} - \frac{\frac{1}{\sigma_n^2} P_c \boldsymbol{v}(f_c, \phi_c) \boldsymbol{v}^{\mathrm{H}}(f_c, \phi_c)}{\sigma_n^2 + M P_c} \right] \tag{10}$$

According to Equation (6), the target adaptive weight vector $\boldsymbol{v}_{stap}$ can be represented as follows:

$$\boldsymbol{v}_{stap} = \mathbf{R}^{-1} \boldsymbol{v}(f_t, \phi_t) = \frac{1}{\sigma_n^2} \left[\boldsymbol{v}(f_t, \phi_t) - \frac{\frac{1}{\sigma_n^2} P_c \boldsymbol{v}(f_c, \phi_c) \boldsymbol{v}^{\mathrm{H}}(f_c, \phi_c) \boldsymbol{v}(f_t, \phi_t)}{\sigma_n^2 + M P_c} \right], \tag{11}$$

where $\frac{1}{M} \boldsymbol{v}^{\mathrm{H}}(f_c, \phi_c) \boldsymbol{v}(f_t, \phi_t)$ can be regarded as the correlation between the space-time steering vectors of the target and the clutter component ρ_{tc}. Thus, $\boldsymbol{v}_{stap}$ is represented as follows:

$$\boldsymbol{v}_{stap} = \frac{1}{\sigma_n^2} \left[\boldsymbol{v}(f_t, \phi_t) - \frac{\frac{M}{\sigma_n^2} P_c \boldsymbol{v}(f_c, \phi_c) \rho_{tc}}{\sigma_n^2 + M P_c} \right]. \tag{12}$$

It can be inferred that v_{stap} is influenced by the clutter-to-noise ratio (CNR) and ρ_{tc}. When the CNR is fixed, the performance of v_{stap} worsens as the correlation ρ_{tc} increases. Consequently, when the energy of clutter components and the correlation with the target are high, the angle and Doppler frequency information of the target after STAP processing will be strongly influenced. The following simulation shows the effect in detail.

The system simulation parameters are listed in Table 1; the main-lobe widths of the angle and Doppler frequency were 23.5° and 0.0242 Hz, respectively. The target was located at 0° with a Doppler frequency of 0 Hz. Figure 1a,b show the correlation between the target and clutter components in the angle and Doppler frequency domains as the clutter component stepped away from the target. The red vertical lines represent the main lobe. When the clutter component was in the main lobe of the target, the correlation coefficient was greater than 0.7 in the angle domain and 0.65 in the Doppler frequency domain, respectively. The effect was even more severe in the angle domain due to the high probability of clutter components in such a wide main lobe.

Table 1. System parameters.

Parameter	Value
λ	53.5 m
d	14.5 m
N_e	8
N_p	512
t_m	20.6 s

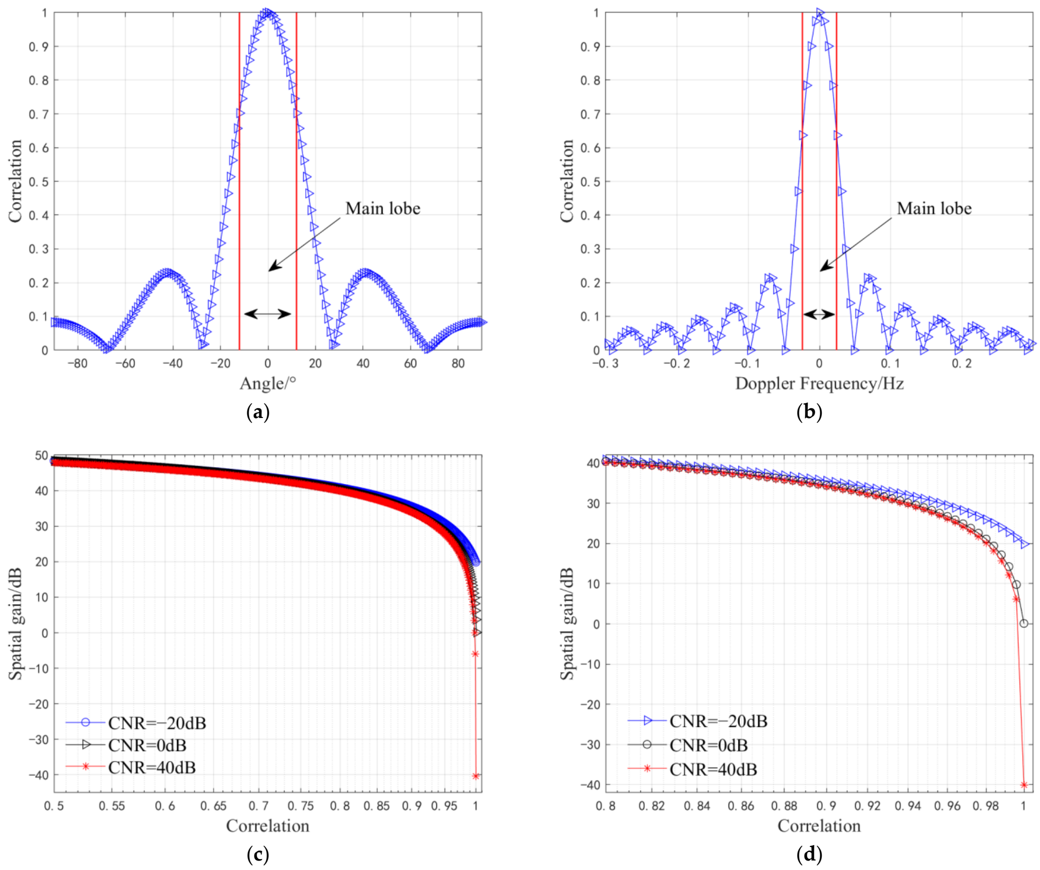

Figure 1. (**a**) Correlation between target and clutter components in the angle domain. (**b**) Correlation between target and clutter components in the Doppler frequency domain. (**c**) Spatial gain in the target direction via the correlation between the clutter component and target for different CNRs. (**d**) Partial enlargement of (**c**).

Figure 1c shows the spatial gain in the target direction via the correlation between the clutter component and the target for different CNRs. The spatial gain here represents the gain in Doppler frequency domain and angle domain. Figure 1d shows a partial enlargement of Figure 1c. The horizontal coordinates in Figure 1d are logarithmic, and the gain of $\boldsymbol{v}_{stap}$ to the target decreased with an increase in the correlation between the target and clutter components, whereas the increase in CNR led to a lower spatial gain. In conclusion, the results of the simulation indicated that the main-lobe clutter seriously influenced the adaptive weight vector $\boldsymbol{v}_{stap}$ response beam pattern of STAP by distorting the beam pattern and reducing the spatial gain.

3. Sparse Representation of the Space-Time Clutter Spectrum

The clutter component should be recognised and separated to avoid its effects in the main lobe. The following content is an algorithm described in our previous work [16] to solve the sparse representation of clutter components, and the results can be used for subsequent calculations.

The space-time plane can be discretised as uniformly integrated points $K = N_{\mathrm{s}} N_{\mathrm{d}}$, where N_{s} and N_{d} represent the numbers of spatial and Doppler frequency bins, respectively. Each grid point is associated with a space-time steering vector $\boldsymbol{v}_k,\ k = [1, 2, \ldots, K]$. The STAP dictionary $\boldsymbol{\Phi} \in \mathbb{C}^{M \times K}$ represents a combination of all these space-time steering entities:

$$\boldsymbol{\Phi} = [\boldsymbol{v}_1, \ldots, \boldsymbol{v}_K]. \tag{13}$$

The training samples can then be represented as follows:

$$\boldsymbol{X}_l = \boldsymbol{\Phi}\gamma_l + \boldsymbol{n}, \tag{14}$$

where $\gamma_l \in \mathbb{C}^{K \times 1}$ is the space-time profile. Equation (14) is the canonical signal form of the sparse-representation problem, which can be interpreted as estimating a sparse vector γ_l with as few nonzero elements as possible.

An iterative compressed sensing method has been developed using the sparse representation of the clutter spectrum without prior information on the sparseness degree [18]. The l_0-norm is expressed as follows:

$$\|\gamma_l\|_0 = \sum_{k=1}^{K} \Gamma(\|\gamma_l(k)\|_2). \tag{15}$$

where $\|\bullet\|_0$ denotes the l_0-norm, which measures the number of nonzero elements in a vector; and $\|\bullet\|_2$ represents the l_2-norm. Because γ_l satisfies sparsity, $\Gamma(\cdot)$ can be defined as follows:

$$\Gamma(t) = \begin{cases} 0, & t = 0 \\ 1, & otherwise \end{cases}. \tag{16}$$

A method for solving this nonsmooth problem has been devised. We also considered that the clutter conformed to the Gaussian law [19]. Hence, we used a Gaussian equation to estimate $\|\gamma_l\|_2$. The Gaussian law is expressed as follows:

$$f_\sigma(\alpha) = \mathrm{e}^{-\alpha^2/2\sigma^2}, \tag{17}$$

where α is the expectation representing the centre of the clutter distribution and σ is the variance in the distribution. When $\alpha \neq 0$ and $\sigma \to 0$, we can determine the minimum solution of l_0-norm $\|\gamma_l\|_0 = K - F_\sigma(\gamma_l)$ using:

$$F_\sigma(\gamma_l) = \sum_{k=1}^{K} f_\sigma(\|\gamma_l(k)\|_2). \tag{18}$$

Here, the result of γ_l can be formulated as the following optimisation problem:

$$\begin{cases} \widehat{\gamma}_l(\sigma) = \operatorname{argmin} L_\sigma(\gamma_l) \\ L_\sigma(\gamma_l) = -F_\sigma(\gamma_l) + \|\mathbf{X}_l - \mathbf{\Phi}\gamma_l\|_2^2 \end{cases} . \tag{19}$$

defining the following equation:

$$\varsigma(\gamma_l) = 2\lambda\left[\frac{\mathbf{W}(\gamma_l)}{\sigma^2} + 2\lambda\mathbf{\Phi}^{\mathrm{H}}\mathbf{\Phi}\right]^{-1}\mathbf{\Phi}^{\mathrm{H}}\mathbf{X}_l, \tag{20}$$

where $\mathbf{W}(\gamma_l) = \operatorname{diag}[f_\sigma(\|\gamma_l(k)\|_2)]$ represents the main components of the clutter and $\operatorname{diag}[\bullet]$ represents the transformation of data into a diagonal matrix.

This method gradually reinforces some of the already prominent entries in the pseudo-inverse operation of the corresponding sparse solution while diminishing the remaining elements until they approach zero and converge. For each γ_l, the real number β satisfies the following expression:

$$L_\sigma\{\beta\varsigma(\gamma_l) + (1-\beta)\gamma_l\} \le L_\sigma(\gamma_l). \tag{21}$$

If Equation (21) is satisfied, we can obtain the optimal γ_l through iterations, where the relationship between iterations (j) and $(j+1)$ can be expressed as follows:

$$\gamma_l^{(j+1)} = \varsigma\left(\gamma_l^{(j)}\right). \tag{22}$$

The result of this iteration can separate the target component from the clutter components, and the clutter components can be used for the subsequent BR calculation.

4. Proposed Method

In this study, the main- and side-lobe clutters of the two-dimensional space-time system were processed separately. The main-lobe clutter was processed via eigen-projection matrix preprocessing (EMP), whereas beam pattern reshaping was used to suppress the side-lobe clutter with strong energy. The principal clutter components obtained using the sparse-representation method, presented earlier, can be divided into the components of the main lobe $\mathbf{C}_m$ and the side lobe $\mathbf{C}_s$.

4.1. Eigen-Projection Matrix Preprocessing Method

The principal component $\mathbf{C}_m$ of the clutter in the main lobe is eigen-decomposed as follows:

$$\widehat{\mathbf{C}_m} = \sum_j^M \lambda_j \boldsymbol{u}_j \boldsymbol{u}_j^{\mathrm{H}} = \mathbf{U}_m \mathbf{\Lambda}_m \mathbf{U}_m^{\mathrm{H}} + \mathbf{U}_n \mathbf{\Lambda}_n \mathbf{U}_n^{\mathrm{H}}, \tag{23}$$

where $\lambda_1 \ge \lambda_2 \ge \ldots \ge \lambda_p \ge \ldots \ge \lambda_M$ are the eigenvalues in descending order, and λ_j u_j denote the j_{th} eigenvalue and eigenvector, respectively, of the principal component $\widehat{\mathbf{C}_m}$ of the clutter in the main lobe. The notation $\mathbf{U}_m = [\boldsymbol{u}_1, \ldots, \boldsymbol{u}_P]$ represents the main-lobe clutter subspace. Moreover, $\mathbf{\Lambda}_s = \operatorname{diag}[\lambda_1, \ldots, \lambda_P]$ represents the eigenvalues, whereas $\mathbf{U}_n = [\boldsymbol{u}_{P+1}, \ldots, \boldsymbol{u}_M]$ denotes the noise subspace and $\mathbf{\Lambda}_n = \operatorname{diag}[\lambda_{P+1}, \ldots, \lambda_M]$.

The adaptive space-time vector pattern can be shaped as the subtraction of eigen beams from the quiescent space-time vector pattern, which can be expressed as follows [20]:

$$G_a(f_t, \phi_t) = G_q(f_t, \phi_t) - \sum_{m=1}^{M} \frac{\lambda_m - \lambda_{\min}}{\lambda_m} \cdot (v_q^{\mathrm{H}} \boldsymbol{u}_m) \cdot G_m(f_t, \phi_t), \tag{24}$$

where $G_q(f_t, \phi_t) = v_q^{\mathrm{H}} v(f_t, \phi_t)$ is the quiescent space-time vector response pattern, v_q is the quiescent space-time vector, $G_m(f_t, \phi_t) = \boldsymbol{u}_m^{\mathrm{H}} v(f_t, \phi_t)$ is the eigen beam of the m_{th}

eigenvector, and $\lambda_{\min}$ denotes the smallest eigenvalue of $\widehat{\mathbf{C}_m}$ [21]. The eigenvector of the two-dimensional main-lobe clutter components $\boldsymbol{u}_m$ is estimated as follows:

$$\left|\boldsymbol{u}_m{}^{\mathrm{H}}\boldsymbol{v}(f_t,\phi_t)\right|^2 = d_s\left|\boldsymbol{v}_q\right|^2, \tag{25}$$

where d_s denotes an appropriate scalar factor. Thus, the eigen-projection matrix is obtained as follows:

$$B = \mathbf{I} - \boldsymbol{u}_m\left(\boldsymbol{u}_m^{\mathrm{H}}\boldsymbol{u}_m\right)^{-1}\boldsymbol{u}_m^{\mathrm{H}}, \tag{26}$$

where $\mathbf{I}$ is the identity matrix. The projection of the training data onto the orthogonal subspace of the clutter components can be expressed as follows:

$$Y = BX. \tag{27}$$

According to the minimum variance principle, the adaptive weight vector can be calculated as follows:

$$\boldsymbol{v}_{MV} = \frac{\widehat{\mathrm{R}}_{\mathrm{Y}}^{-1}\boldsymbol{v}(f_t,\phi_t)}{\boldsymbol{v}^{\mathrm{H}}(f_t,\phi_t)\widehat{\mathrm{R}}_{\mathrm{Y}}^{-1}\boldsymbol{v}(f_t,\phi_t)}, \tag{28}$$

where $\widehat{\mathrm{R}}_Y$ denotes the sample covariance matrix of the processed data Y. The Doppler frequency and azimuth of the desired signal correspond to f_t and ϕ_t, respectively. Thus, $\boldsymbol{v}(f_t,\phi_t)$ is the space-time vector of the desired signal.

4.2. Space-Time Beam Pattern Reshaping

The adaptive space-time vector based on the minimum variance principle is typically defined as the solution to the following linearly constrained minimisation problem [22]:

$$\begin{cases} v = \underset{w}{\operatorname{argmin}}(\boldsymbol{v}^{\mathrm{H}}\mathbf{R}v) \\ \text{s.t. } \boldsymbol{v}^{\mathrm{H}}\boldsymbol{v}(f_t,\phi_t) = 1 \end{cases}, \tag{29}$$

where $\boldsymbol{v}$ represents the space-time vector and $\boldsymbol{v}^{\mathrm{H}}\boldsymbol{v}(f_t,\phi_t) = 1$ denotes the distortionless constraint applied to the desired signal. However, this result becomes inconsistent when clutter is present in the main lobe. To shape the two-dimensional beam pattern, the main lobe of the adaptive space-time and quiescent space-time patterns should be as similar as possible. The space-time vector of the main lobe $\boldsymbol{v}_m$ is expressed as follows:

$$\boldsymbol{v}_m = \underset{v}{\operatorname{argmin}}\|\boldsymbol{v} - \boldsymbol{v}_q\|^2. \tag{30}$$

In addition, high side-lobe levels are a significant disadvantage of beamforming. Thus, the following cost function was proposed to minimise the side lobe:

$$\boldsymbol{v}_s = \underset{v}{\operatorname{argmin}}\|\boldsymbol{v}^{\mathrm{H}}\boldsymbol{\Phi}_s\|^2, \tag{31}$$

where $\boldsymbol{v}_s$ denotes the space-time vector of the side lobe, $\boldsymbol{\Phi}_s = [v_{s1},\ldots,v_{sK_s}]$ denotes the set of all side-lobe space-time vectors, and K_s is the number of side-lobe space-time vectors. To suppress the side-lobe clutter, the objective function to shape the beam pattern can be constructed as follows:

$$\begin{cases} v = \underset{v}{\operatorname{argmin}}\|\boldsymbol{v} - \boldsymbol{v}_q\|^2 + \mu_s\|\boldsymbol{v}^{\mathrm{H}}\boldsymbol{\Phi}_s\|^2 \\ \text{s.t.}\mathbf{C}_s{}^{\mathrm{H}}\boldsymbol{v} = \mathbf{f} \end{cases}, \tag{32}$$

where $\mathbf{C}_s = [\boldsymbol{v}(f_t,\phi_t),\boldsymbol{v}(f_{c1},\phi_{c1}),\ldots,\boldsymbol{v}(f_{cQ},\phi_{cQ})]$ and $\boldsymbol{v}(f_{c1},\phi_{c1}),\ldots,\boldsymbol{v}(f_{cQ},\phi_{cQ})$ denote the space-time vectors of the side-lobe clutter components, whereas Q is the number of clutter components in the side lobe. Exact clutter components can be obtained from the sparse-representation results. In addition, μ_s is a weighting factor that balances similarity constraints. Here, $\mathbf{f} = [g_t, g_1, \ldots, g_q, \ldots, g_Q]$ is a constraint vector, where g_t is the gain coefficient of the target space-time vector, which is usually 1. In contrast, g_q is the gain coefficient of the q_{th} clutter component, which can be calculated based on the magnitudes of the clutter components:

$$g_q = \frac{\mu_c}{\mathrm{A}_{cq}}, \tag{33}$$

where g_q is inversely proportional to the magnitude of the estimated clutter components A_{cq} and $g_s < 1$, whereas μ_c is a weighting factor that controls clutter-suppression performance. The proposed optimisation model is a convex objective function that can be solved using a convex optimisation solver. The adaptive weight vector can be obtained using the Lagrange multiplier method, which is expressed as follows:

$$\mathbf{J}(v) = \|\boldsymbol{v} - \boldsymbol{v}_q\|^2 + \mu_s \|\boldsymbol{v}^{\mathrm{H}} \boldsymbol{\Phi}_s\|^2 + \Re\Big\{ {\eta_s}^{H} ({\mathbf{C}_s}^{\mathrm{H}} \boldsymbol{v} - \mathbf{f}) \Big\}, \tag{34}$$

where $\Re\{\bullet\}$ denotes the real part of the operator and η_s is the Lagrange multiplier vector. Thus:

$$\nabla \mathbf{J}(v) = 2v - 2v_q + \mu_s \boldsymbol{\Phi}_s {\boldsymbol{\Phi}_s}^H v + 2\mathbf{C}_s \lambda. \tag{35}$$

When $\nabla \mathbf{J}(v) = 0$,

$$\boldsymbol{v} = \left(\boldsymbol{\Phi}_s {\boldsymbol{\Phi}_s}^H + \mathbf{I}\right)^{-1} (\boldsymbol{v}_q - \mathbf{C}_s \lambda), \tag{36}$$

When (36) is substituted into ${\mathbf{C}_s}^{\mathrm{H}} v = \mathbf{f}$:

$${\mathbf{C}_s}^{\mathrm{H}} \left(\boldsymbol{\Phi}_s {\boldsymbol{\Phi}_s}^{\mathrm{H}} + \mathbf{I}\right)^{-1} (v_q - \mathbf{C}_s \lambda) = \mathbf{f}. \tag{37}$$

Thus, the λ can be expressed as:

$$\lambda = \left({\mathbf{C}_s}^{\mathrm{H}} \left(\boldsymbol{\Phi}_s {\boldsymbol{\Phi}_s}^{\mathrm{H}} + \mathbf{I}\right)^{-1} \mathbf{C}_s\right)^{-1} \left({\mathbf{C}_s}^{\mathrm{H}} \left(\boldsymbol{\Phi}_s {\boldsymbol{\Phi}_s}^{\mathrm{H}} + \mathbf{I}\right)^{-1} \boldsymbol{v}_q - \mathbf{f}\right). \tag{38}$$

When (38) is substituted into (37):

$$v_{opt} = \Xi^{-1} \left(\left(\mathbf{I} - \mathbf{C}_s \left({\mathbf{C}_s}^{\mathrm{H}} \Xi^{-1} \mathbf{C}_s\right)^{-1} {\mathbf{C}_s}^{\mathrm{H}} \Xi^{-1} \right) \boldsymbol{v}_q - \mathbf{C}_s \left({\mathbf{C}_s}^{\mathrm{H}} \Xi^{-1} \mathbf{C}_s\right)^{-1} \mathbf{f} \right), \tag{39}$$

where

$$\Xi = \mu_s \boldsymbol{\Phi}_s {\boldsymbol{\Phi}_s}^{\mathrm{H}} + \mathbf{I}. \tag{40}$$

Thus, we obtain the result for v_{opt}, which is the optimal adaptive space-time vector of the proposed method. Finally, the output of the clutter suppression was calculated as follows:

$$Z = {\boldsymbol{v}_{opt}}^H Y. \tag{41}$$

This result ensured that the main lobe of the desired Doppler frequency and direction produced the least distortion and was not influenced by the clutter components in the side lobe.

4.3. Algorithm

The algorithm flow can be summarised as follows (Algorithm 1):

Algorithm 1. Beam Reshaping

Sparse representation algorithm
Initialization process:
$\gamma_l{}^{(0)} = \mathbf{\Phi}^{\mathrm{H}}\left(\mathbf{\Phi}\mathbf{\Phi}^{\mathrm{H}}\right)^{-1}\boldsymbol{X}_l$
$\sigma^{(0)} = \max\|\gamma_l{}^{(0)}\|_1$
$\sigma_0 \in \left[0.1,\ 10^{-4}\right]$
where μ and η are coefficients of convergence.
for each j-th iteration process:
When $L_\sigma\left\{\beta\varsigma\left(\gamma_l{}^{(j)}\right) + (1-\beta)\gamma_l{}^{(j)}\right\} > L_\sigma\left(\gamma_l{}^{(j+1)}\right)$,
Update $\beta = \eta\beta$ and $\gamma_l{}^{(j+1)} = \beta\varsigma\left(\gamma_l{}^{(j)}\right) + (1-\beta)\gamma_l{}^{(j)}$
When $\|\gamma_l{}^{(j+1)} - \varsigma\left(\gamma_l{}^{(j)}\right)\|_2 < \eta\sigma$
Update $\sigma = \mu\sigma$
end if
$\sigma < \sigma_0$
obtain γ_l.
Divide the principal components γ_l of the clutter into the main lobe clutter $\mathbf{C}_m$ and side-lobe clutter $\mathbf{C}_s$.
Use $\mathbf{C}_m$ to construct the covariance matrix for eigen decomposition to obtain $\mathbf{U}_m = \left[\boldsymbol{u}_1, \ldots, \boldsymbol{u}_p\right]$.
Calculate the weight vector $\boldsymbol{v}_{MV}$.
Use $\boldsymbol{v}_{MV}$ as the quiescent space-time vector $\boldsymbol{v}_q$ in the following calculation.
Construct the constraint vector $\mathbf{f}$ based on $\mathbf{C}_s$.
Calculate the adaptive space-time steering vector $\boldsymbol{v}_{opt}$.

5. Simulation Results

Two approaches were used to evaluate the performance of the proposed algorithm. The first approach used simulation data for the algorithm evaluation, whereas the second approach injected simulation targets into the measured data. The proposed algorithm results were compared and evaluated against the quiescent space-time vector, standard STAP, and SR-STAP in terms of performance. To improve the accuracy of the Doppler frequency, a second-order polynomial fitting was used to calculate the peak value. The SR-STAP used here was STAP processing based on space-time training samples processed by the sparse-representation algorithm in Section 3. In cases involving clutter components that included both the main lobe and side lobe, the performance of the algorithm in preventing the main-lobe distortion of the target was based primarily on the response pattern of the adaptive weight vector v in the target direction. That is, the adaptive weight vector $\boldsymbol{v}_{opt}$ was matched with all space-time vectors.

5.1. Simulation Data

For the simulation, we set the system parameters as summarised in Table 1. The grid density in the spatial and Doppler frequency domains were 3° and 0.0970 Hz, respectively. We set the sparse-representation algorithm parameters as: $N_{\mathrm{d}} = 151$, $N_{\mathrm{s}} = 91$, $\beta = 1$, $\eta = 0.5$, $\mu = 0.3$, $\sigma_0 = 0.01$, and $L = 2$. Furthermore, we set the BR algorithm parameters as: $\mu_s = 1$, $\mu_c = 0.01$ and $\eta_s = 1$.

Because principal clutter components could be estimated using the sparse-representation algorithm, several space-time vectors were set as principal clutter components during the simulation. The parameters of the clutter components and target are shown in Table 2. The width of the main lobe was approximately 23.5° under the system parameters. Thus, components 1 and 2 in Table 2 denote the main-lobe clutter in both the angle and Doppler frequency domains, whereas components 3 to 7 denote the side-lobe clutter. Gaussian noise with a signal-to-noise ratio (SNR) of 20 dB was added as the background. The clutter amplitude was measured using the CNR.

Table 2. Clutter components and target simulation parameters.

	Doppler Frequency (Hz)	Angle	SNR/CNR (dB)	Main/Side Lobe
Target	−1.116	0°	20	
Clutter component 1	−1.116	9°	23	Main lobe
Clutter component 2	−1.099	0°	23	Main lobe
Clutter component 3	−1.116	−39°	20	Side lobe
Clutter component 4	−1.116	30°	23	Side lobe
Clutter component 5	−0.825	−39°	20	Side lobe
Clutter component 6	−0.825	30°	23	Side lobe
Clutter component 7	−1.309	−6°	23	Side lobe

Figure 2a shows the angle–Doppler map of data under the simulation conditions. It can be observed that the target was drowning in clutter. Figure 2b,c show the target angle and Doppler frequency domains, respectively. The red dotted line is the target location. Because strong clutter components existed in the main and side lobe, the peak of the target in the angle domain deviated. The peak of the target was also at the inaccurate Doppler frequency. These deviations seriously influenced the estimation of target information.

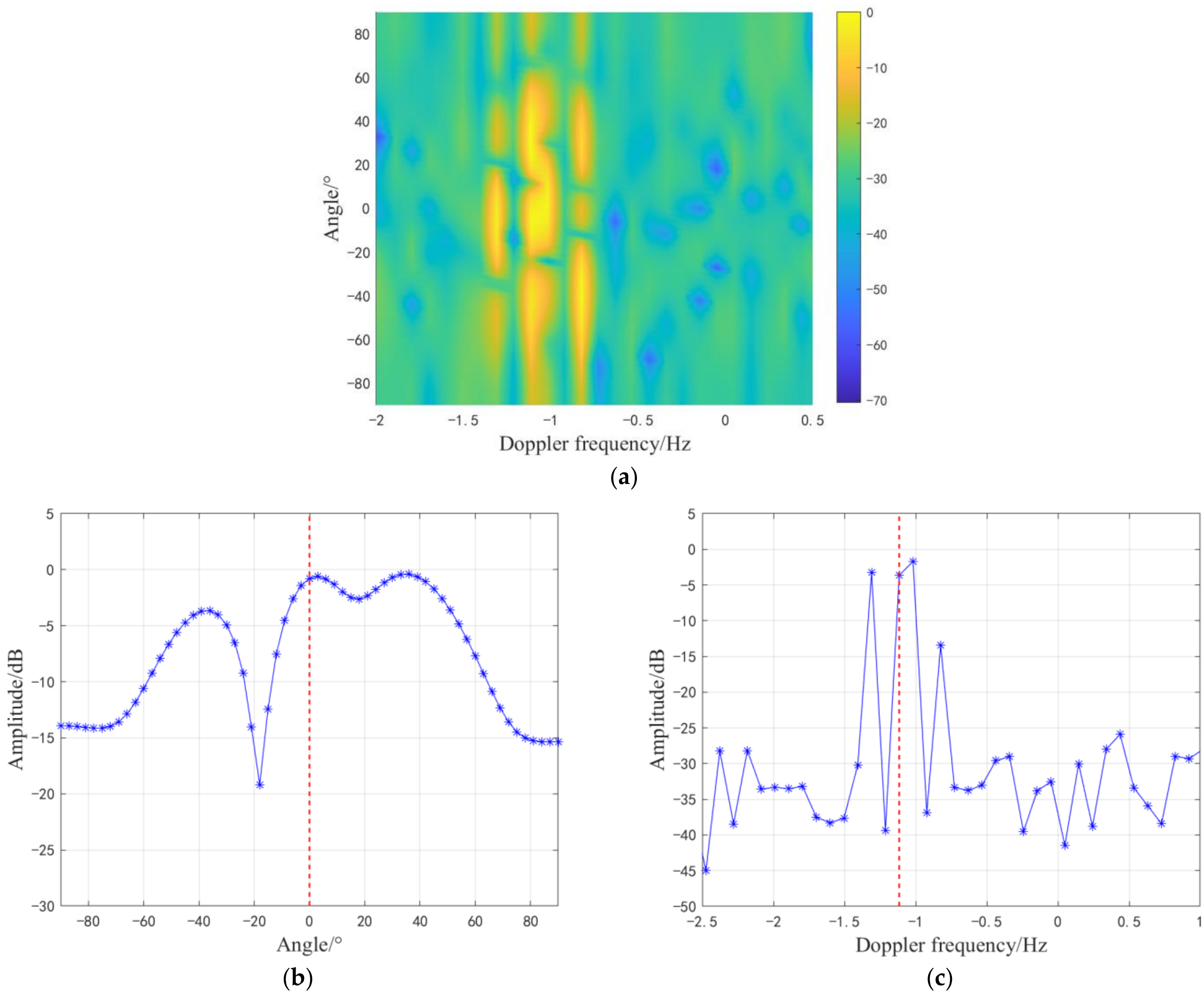

Figure 2. (**a**) Angle–Doppler map of simulation data; (**b**) angle domain curve at the target Doppler frequency; and (**c**) Doppler frequency curve in the target angle.

Figure 3a,b show comparisons between the response patterns of the weight vector in the angle and Doppler frequency domains for different algorithms using the simulated data shown in Figure 2. As shown in Figure 3a, in the response of the STAP algorithm, the main lobe was offset by $-2.9°$, resulting in poor performance in suppressing the side-lobe clutter components. In contrast, the response of the SR-STAP algorithm had the narrowest main-lobe width, which had the best gain for the target direction. However, the resulting angle was inaccurate, and was offset by $-3°$. The main-lobe pattern from the BR method proposed in this study was highly similar to the result of the quiescent space-time vector, and the peak was accurate. Moreover, deep notches existed at $-39°$ and $30°$ at the angles of the clutter components due to the BR.

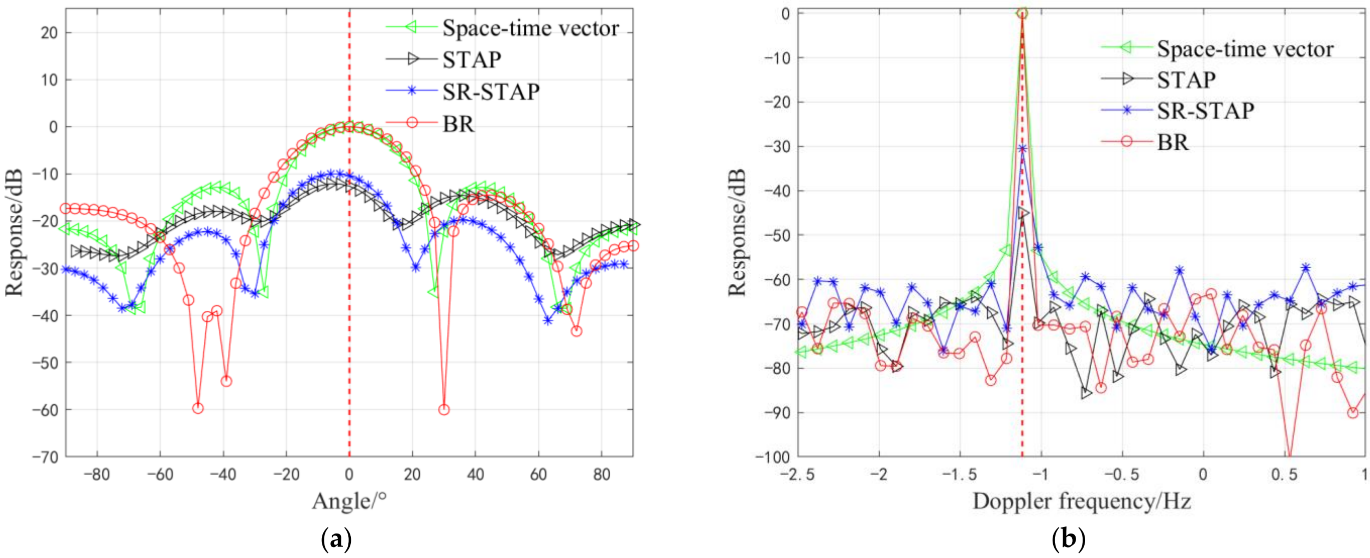

Figure 3. Comparison of response patterns for the weight vector in (**a**) the angle domain and (**b**) the Doppler frequency domain for different algorithms.

According to Figure 3b, the standard STAP algorithm exhibited no evident suppression in the Doppler frequency domain, whereas the offset of the peak was -0.020 Hz by second-order polynomial fitting. The SR-STAP algorithm had a certain suppression effect in the Doppler frequency domain. Nevertheless, the peak frequency was inaccurate; that is, it was offset by -0.0912 Hz. In contrast, the BR algorithm had a good suppression effect on clutter components, with the lowest offset of 0.001 Hz, and it had the highest gain, which was 30.9 and 45.5 dB higher than that of SR-STAP and STAP, respectively. The BR algorithm proposed in this study had a better performance than the quiescent space-time vector.

To fully illustrate the effect of the main-lobe clutter on the angle offset of the response pattern, the following experiments were performed. We set clutter component 1 with different energies and angles (10−40 dB and 0−12°, respectively), and the Monte Carlo experiment was run 1000 times. The results of the angle offset varying with the energy and angle of the main-lobe clutter are shown in Figure 4a,b, respectively. As shown in Figure 4a, the angle offset of the beam pattern from the STAP and SR-STAP algorithms increased with an increase in the main-lobe clutter amplitude. As shown in Figure 4b, the angle offset increased with the clutter angle, but decreased after it increased to a certain angle. In contrast, the response pattern of BR was not influenced by the change in amplitude and angle of the main-lobe clutter, and was always accurate.

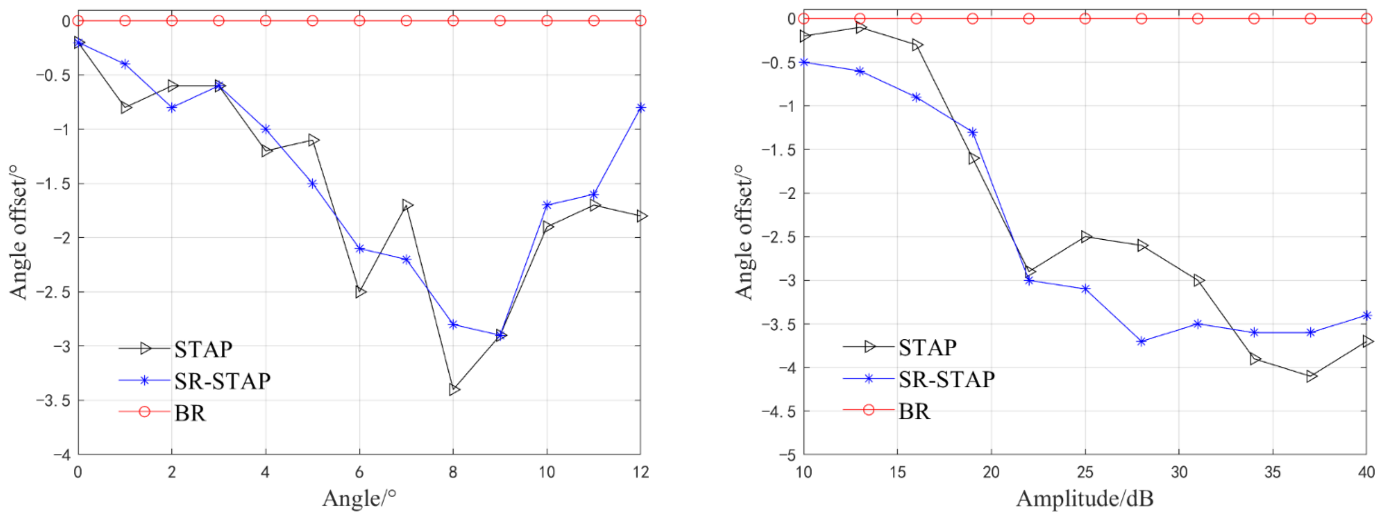

(**a**) (**b**)

Figure 4. Result of the angle offset varying with (**a**) the energy of the main-lobe clutter and (**b**) the angle of the main-lobe clutter.

5.2. Measured Data

The experimental parameters for the measured data are outlined in Table 3. In this section, a simulation target was injected into the measured data. The target was set at the No. 94 range bin, the angle was 21°, and the Doppler frequency was set to 0.279 Hz. The signal-to-clutter ratio of the target was 0 dB. The grid density in the spatial and Doppler frequency domains were 3° and 0.0485 Hz, respectively. We set the sparse-representation algorithm parameters as: $N_d = 251$, $N_s = 61$, $\beta = 1$, $\eta = 0.5$, $\mu = 0.3$, $\sigma_0 = 0.01$, and $L = 2$. Furthermore, we set the BR algorithm parameters as: $\mu_s = 1$, $\mu_c = 0.01$, and $\eta_s = 1$.

Table 3. System parameters of measured data.

Parameter	Value
λ	53.5 m
d	14.5 m
N_e	8
N_p	1024
t_m	41.2 s

Figure 5a shows the range–Doppler map of the measured data. The ionospheric clutter and sea clutter are also labelled. It can be seen that the ionospheric clutter had a high intensity and was widely distributed over the Doppler frequency domain and range domain. The ionospheric clutter near the No. 94 range bin was used in this experiment. The angle–Doppler map of the No. 94 range bin is shown in Figure 5b. The target was obscured by the clutter. In this case, the ionospheric clutter seriously affected the accuracy of target detection. Figure 5c,d show the target angle and Doppler frequency domains, respectively. The red dotted line is the target location. Three pairs of vertical lines indicate the range of clutter, and can be seen from −78° to −42°, from −20° to 40°, and from 57° to 78° in the angle domain. In the Doppler frequency domain, the clutter spread from 0.09 to 0.450 Hz. The angle and Doppler frequency of the target shifted due to the clutter, making it difficult to detect the target information.

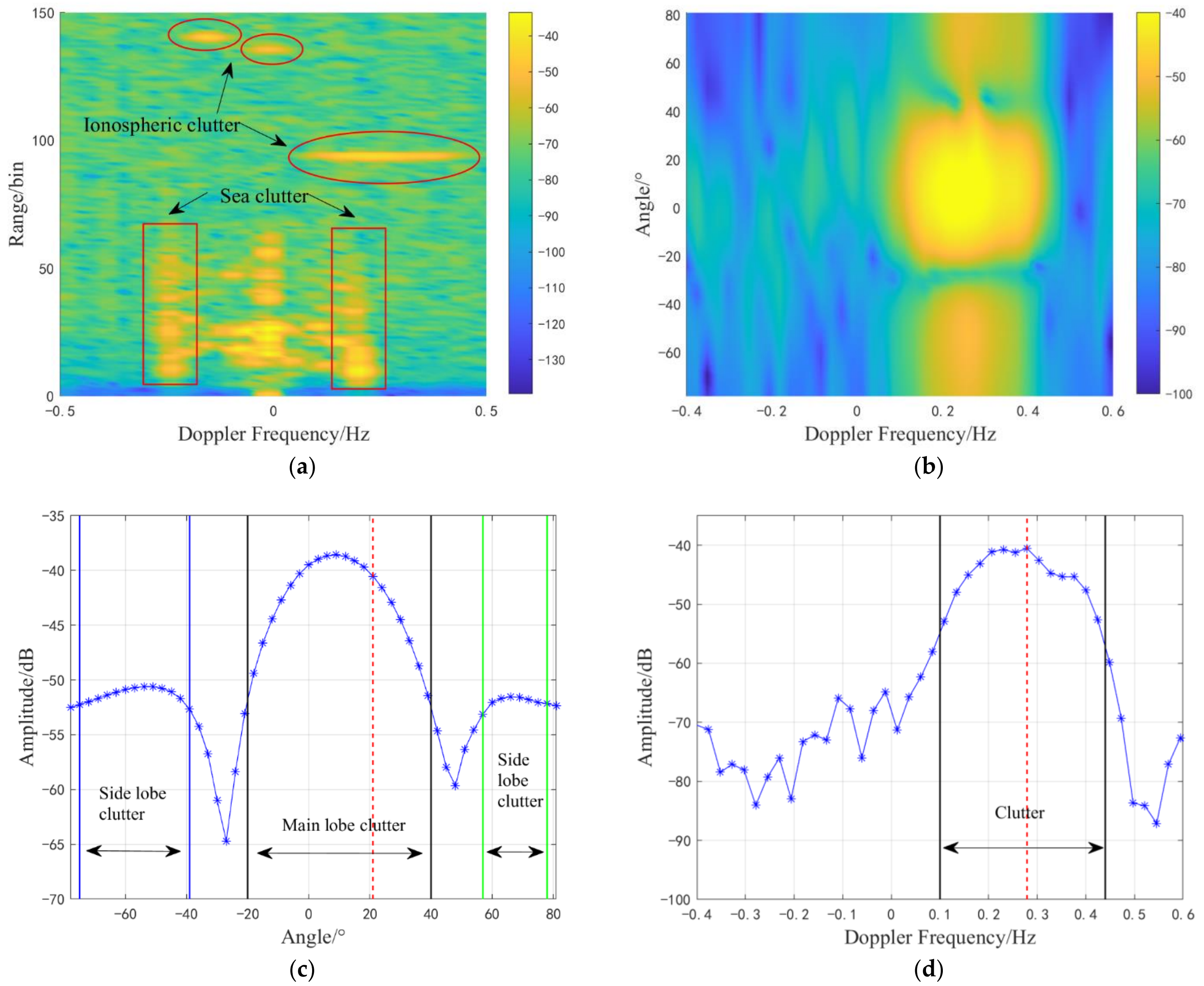

Figure 5. (**a**) Range–Doppler map of the measured data; (**b**) angle–Doppler map of the measured data; (**c**) angle curve at the Doppler frequency of the target; and (**d**) the Doppler frequency curve at the angle of the target.

Figure 6a shows the angle–Doppler map of the No. 94 range bin using the sparse-representation algorithm mentioned in Section 3, which contained target and clutter components. The target is marked with red lines. Compared to Figure 5c, the sparse principal component could separate the target from the clutter. Figure 6b shows the angle–Doppler map of the No.95 range bin as an example of adjacent range bins, which contained only clutter components. The components with the same distribution in adjacent distance elements were selected as clutter components. The clutter was contained in the main and side lobe, which could be used as clutter space-time vectors in the BR algorithm. The main-lobe clutter was distributed around 12°, and the side-lobe clutter was distributed around −57° and 51°. These components were used in subsequent BR calculation.

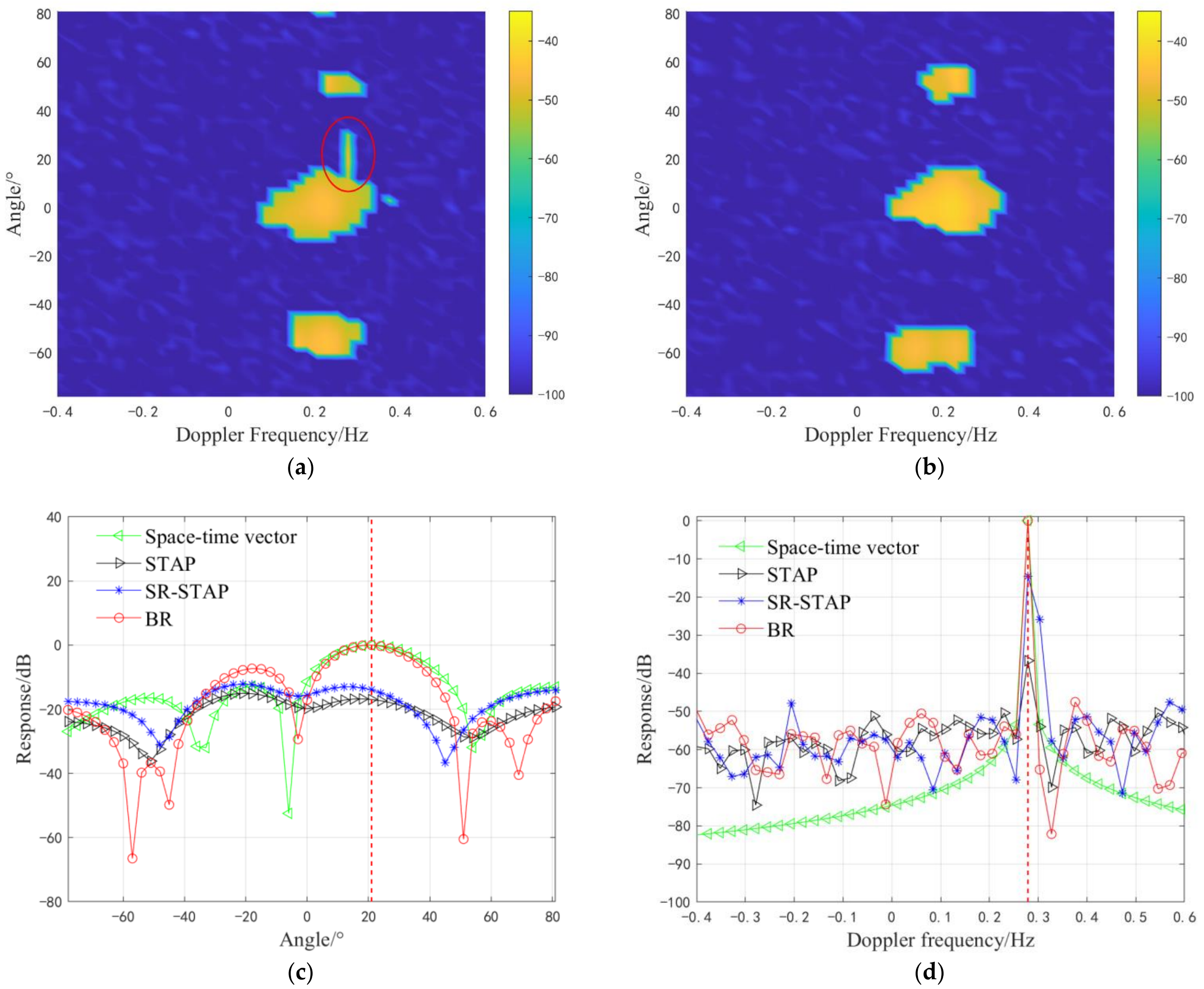

Figure 6. (**a**,**b**) Angle–Doppler maps of the No. 94 and No. 95 range bins after sparse representation. Comparison of response patterns for the weight vector in (**c**) the angle domain and (**d**) Doppler frequency domain for different algorithms for the measured data.

Figure 6c,d show a comparison between the response patterns of the weight vector in the angle and Doppler frequency domains for the different algorithms for the measured data. As shown in Figure 6c, the response pattern of the STAP was similar to those obtained in the simulation experiment. This could not guarantee the accuracy of the main-lobe peak, which was offset by −2.8°, nor the suppression of the side-lobe clutter components. The SR-STAP algorithm could have a narrow main-lobe width; however, the peak angle was incorrect, and was offset by −4.9°. Moreover, there was no clear suppression of the side-lobe clutter area. However, the beam pattern of the main lobe from the BR was similar to that of the quiescent space-time vector, and the peak was accurate. In addition, there were notches at −57° and 51°, which were consistent with the estimated clutter distribution, and could suppress the clutter component of the side lobe.

According to Figure 6d, the peak of STAP was offset by 0.021 Hz. In addition, the peak of SR-STAP was offset by 0.011 Hz. Nonetheless, the BR algorithm better suppressed the clutter components, with the lowest offset of 0.001 Hz, and it had the highest gain of 26.0 and 37.6 dB higher than that of SR-STAP and STAP, respectively. Among the tested algorithms, the proposed BR algorithm had the best suppression performance and the most accurate main-lobe peak response.

6. Conclusions

This study analysed and confirmed that the clutter components in the main lobe of the target caused its deformation during STAP processing, resulting in a loss of the angle and Doppler frequency information of the target after clutter suppression. Then, a STAP clutter-suppression method was proposed based on BR for HFSWR. The algorithm could maximally suppress the clutter components of the side lobe while ensuring that the main-lobe beam pattern was not deformed by the main-lobe clutter component. Compared with the quiescent space-time vector, standard STAP, and SR-STAP, the proposed BR algorithm provided a more accurate angle–frequency response, which met the requirements of the maximum target response and a notch response with side-lobe clutter, especially in the angle domain. Two approaches were used to evaluate the performance of the proposed algorithm. The first approach used simulation data for the algorithm evaluation, whereas the second approach injected simulation targets into the measured data. In HFSWR, the proposed BR clutter-suppression algorithm could effectively remove the effect of ionospheric clutter and protect the information of the target, which can assist with target detection and tracking despite a background with ionospheric clutter.

There is still potential to considerably improve BR. In particular, although the BR algorithm could completely protect the angle and Doppler frequency information of the target, it could not completely eliminate high-energy clutter from the main lobe. Consequently, it retained part of main-lobe clutter energy, which made it difficult to obtain an extremely high signal-to-clutter ratio. Therefore, a method to eliminate high-energy clutter in the main lobe is required. We will evaluate improving the performance of BR to suppress clutter in the main lobe or develop a method to deal with the main-lobe clutter following BR processing.

Author Contributions: Methodology, validation, writing—original draft preparation, J.L.; software, data curation, validation, X.J. and D.X.; supervision, X.Z.; funding acquisition, Q.Y. All authors have read and agreed to the published version of the manuscript.

Funding: This work was supported by National Natural Science Foundation of China (No. 61701140) and the Fundamental Research Funds for the Central Universities.

Data Availability Statement: Restrictions apply to the availability of the data, which were used under license for this study. Data are available from the authors with permission from the Key Laboratory of Marine Environmental Monitoring and Information Processing.

Acknowledgments: The authors truly thank the Key Laboratory of Marine Environmental Monitoring and Information Processing, Harbin Institute of Technology, China, for data support.

Conflicts of Interest: No author has financial or other contractual agreements that might cause a conflict of interest.

References

1. Li, Q.; Zhang, W.; Li, M.; Niu, J.; Wu, Q.M. Automatic detection of ship targets based on wavelet transform for HF surface wavelet radar. *IEEE Geosci. Remote Sens. Lett.* **2017**, *14*, 714–718. [CrossRef]
2. Barrick, D.E. History, Present Status, and Future Directions of HF Surface-Wave Radars in the U.S. In Proceedings of the 2003 International Conference on Radar (IEEE Cat. No. 03EX695), Adelaide, Australia, 3–5 September 2003.
3. Ponsford, A.; Mckerracher, R.; Ding, Z.; Moo, P.; Yee, D. Towards a cognitive radar: Canada's third-generation high frequency surface wave radar (HFSWR) for surveillance of the 200 nautical mile exclusive economic zone. *Sensors* **2017**, *17*, 1588.
4. Luo, Z.; He, Z.; Chen, X.; Lu, K. Target location and height estimation via multipath signal and 2D array for sky-wave over-the-horizon radar. *IEEE Trans. Aerosp. Electron. Syst.* **2016**, *52*, 617–631. [CrossRef]
5. Chen, S.Y.; Gill, E.W.; Huang, W.M. A high-frequency surface wave radar ionospheric clutter model for mixed-path propagation with the second-order sea scatter. *IEEE Trans. Antennas Propag.* **2016**, *64*, 5373–5381. [CrossRef]
6. Jiang, W.; Deng, W.B.; Shi, J.L. Characteristic Study of Ionospheric Clutter in High-Frequency over the Horizon Surface Wave Radar. In Proceedings of the IEEE Youth Conference on Information, Computing and Telecommunication, Beijing, China, 20–21 September 2009.
7. David, K.B.; Leonov, S.A. *Radar Technology Encyclopedia*; Barton, D., Leonov, S.A., Eds.; Artech House Press: Norwood, MA, USA, 1997; Volume 3, pp. 310–311, ISBN-13 978-1580532594.

8. Hua, X.; Ono, Y.; Peng, L.; Cheng, Y.; Wang, H. Target detection within nonhomogeneous clutter via total Bregman divergence-based matrix information geometry detectors. *IEEE Trans. Signal Process.* **2021**, *69*, 4326–4340. [CrossRef]
9. Hua, X.; Peng, L. MIG median detectors with manifold filter. *Signal Process.* **2021**, *188*, 108176. [CrossRef]
10. Hua, X.; Ono, Y.; Peng, L.; Xu, Y. Unsupervised Learning Discriminative MIG Detectors in Nonhomogeneous Clutter. *IEEE Trans. Commun.* **2022**, *70*, 4107–4120. [CrossRef]
11. Li, Y.; Wei, Y.; Xu, R. An ionospheric Es layer clutter model and suppression in HF surfacewave radar. *Int. J. Antennas Propag.* **2013**, *2013*, 141–169. [CrossRef]
12. Brennan, L.E.; Reed, L.S. Theory of adaptive radar. *IEEE Trans. Aerosp. Electron. Syst.* **1974**, *9*, 853–863. [CrossRef]
13. Ravan, M.; Saleh, O.; Adve, R.S. *KB-STAP Implementation for HFSWR*; Final Report for Defense Research and Development Canada; w7714-060999/001/SV; Dept. of Electrical and Computer Engineering University of Toronto: Toronto, ON, Canada, 2008. Available online: https://www.comm.utoronto.ca/~{}rsadve/Publications/FinalReport.pdf (accessed on 9 July 2021).
14. Adve, R.S.; Hale, T.B.; Wicks, M.C. Practical joint domain localised adaptive processing in homogeneous and nonhomogeneous environments. Part 2: Nonhomogeneous environments. *IEE Proc. Radar Sonar Navig.* **2000**, *147*, 66–74. [CrossRef]
15. Tang, B.; Tang, J.; Peng, Y. Detection of heterogeneous samples based on loaded generalized inner product method. *Digit. Signal Process.* **2012**, *22*, 605–613. [CrossRef]
16. Rabideau, D.J.; Steinhardt, A.O. Improved adaptive clutter cancellation through data-adaptive training. *IEEE Trans. Aerosp. Electron. Syst.* **1999**, *35*, 879–891. [CrossRef]
17. Li, J.; Yang, Q.; Zhang, X.; Guo, L.; Liang, C.; Bai, Y. A STAP clutter suppression algorithm based on sparse representation for small-array HFSWR. *Remote Sens. Lett.* **2022**, *13*, 611–620. [CrossRef]
18. Sun, K.; Meng, H.; Wang, Y.; Wang, X. Direct data domain STAP using sparse representation of clutter spectrum. *Signal Process.* **2011**, *91*, 2222–2236. [CrossRef]
19. Mohimani, H.; Babaie-Zadeh, M.; Jutten, C. A fast approach for overcomplete sparse decomposition based on smoothed norm. *IEEE Trans. Signal Process.* **2009**, *16*, 624–634. [CrossRef]
20. Li, R.; Wang, Y.; Wan, S. Research of reshaping adapted pattern under mainlobe interference conditions. *Mod. Radar* **2002**, *24*, 50–55.
21. Carlson, B.D. Covariance matrix estimation errors and diagonal loading in adaptive arrays. *IEEE Trans. Aerosp. Electron. Syst.* **1988**, *24*, 397–401. [CrossRef]
22. Liu, Y.; Wan, Q. Sidelobe suppression for robust Capon beamforming with mainlobe to sidelobe power ratio maximization. *IEEE Antennas Wirel. Propag. Lett.* **2008**, *11*, 1218–1221. [CrossRef]